# Atmospheric gravity wave effects on polar mesospheric clouds: A comparison of numerical simulations from CARMA 2D with AIM observations

A. Chandran,[1,2,3] D. W. Rusch,[1] G. E. Thomas,[1] S. E. Palo,[2] G. Baumgarten,[4] E. J. Jensen,[5] and A. W. Merkel[1]

[1]  The effects of atmospheric gravity waves (AGWs) on Polar Mesospheric Cloud (PMC) evolution and brightness are studied using a two dimensional version of the Community Aerosol and Radiation Model for Atmospheres (CARMA 2D). The primary objectives for doing CARMA modeling of AGW effects on PMCs are to address the question of whether AGWs can account for the rapid, orbit by orbit changes in cloud structure and brightness seen in overlapping regions from images of the Cloud Imaging and Particle Size (CIPS) experiment on board the Aeronomy of Ice in the Mesosphere (AIM) spacecraft. We present comparisons of PMC brightness changes between our numerical simulations and observations from the CIPS experiment. Previous modeling studies have indicated a much longer life-time for PMC than the 90 min between CIPS orbits. We present CARMA 2D results showing dependence of ice particle growth and PMC brightness on AGW perturbation of background temperatures and water vapor concentrations. The model shows differences in brightness of PMCs due to differences in number of large ice particles depending on the scale and periods of the AGWs and also indicates that overall cloud brightness is a function of the wave period. While the maximum rate of change in PMC brightness from the model is still almost a factor of two less than the CIPS observed maximum rate of change in brightness, our study indicates that the variation in PMC brightness is in part due to the upward transport of water vapor into water depleted region by AGWs and the growth of ice particles from sub visual to visual and to larger sizes than they normally would have without AGWs. The presence of short period AGW cause periodic oscillations in cloud brightness about the no-AGW brightness while long-period AGW can temporarily increase the brightness of PMCs compared to the PMC brightness under no-AGW case. However, both the short-period and long-period AGW ultimately reduce the domain averaged PMC brightness in the long-term. This agrees with CIPS observations of generally dimmer PMCs in regions of high AGW activity. The seasonal variation in PMC albedos and the day to day variations seen in CIPS can be reproduced using a spectrum of short and long period AGW.

**Citation:** Chandran, A., D. W. Rusch, G. E. Thomas, S. E. Palo, G. Baumgarten, E. J. Jensen, and A. W. Merkel (2012), Atmospheric gravity wave effects on polar mesospheric clouds: A comparison of numerical simulations from CARMA 2D with AIM observations, *J. Geophys. Res.*, *117*, D20104, doi:10.1029/2012JD017794.

## 1. Introduction

[2]  Noctilucent Clouds (NLCs) or Polar Mesospheric Clouds (PMCs), as they are known from space-based observations are high altitude ice-clouds that form in the summer polar mesosphere at ∼82 km. PMCs are believed to have been first sighted in the latter part of the 19th century and were first reported in literature by *Leslie* [1885] as a phenomenon of wave-like silvery clouds high up in the atmosphere observed after sunset and before sunrise. The formation of the cold summer mesopause is dynamically driven primarily by atmospheric gravity waves (AGWs) [*Holton*, 1983; *Garcia and Solomon*, 1985]. The temperature of the summertime polar mesopause region is typically

[1]Laboratory for Atmospheric and Space Physics, University of Colorado Boulder, Boulder, Colorado, USA.
[2]Department of Aerospace Engineering Sciences, University of Colorado Boulder, Boulder, Colorado, USA.
[3]Geophysical Institute and Department of Atmospheric Sciences, University of Alaska Fairbanks, Fairbanks, Alaska, USA.
[4]Leibniz-Institute of Atmospheric Physics at Rostock University, Kühlungsborn, Germany.
[5]NASA AMES Center, San Francisco, California, USA.

Corresponding author: A. Chandran, Geophysical Institute, University of Alaska Fairbanks, Fairbanks, AK 80027, USA. (chandran@ucar.edu)

in the range 125–145 K at the mesopause [*Lübken*, 1999]. At these low temperatures, the water vapor content of a few parts per million by volume (ppm$_v$) [*Seele and Hartogh*, 1999] can create a supersaturated gas phase environment conducive to ice particle nucleation and growth. Hence these unique conditions lead to the formation of PMCs during a three-month period around solstice in the summer mesosphere. *Rapp and Thomas* [2006] provided a review of the microphysics of PMCs, and a model study describing a high sensitivity of PMC properties to temperature.

[3] AGWs are known to be the main cause of extensive wave structures often evident in NLCs [*Hines*, 1968] which vary from small-scale wave patterns termed *billows*, with horizontal spacing of ∼3 to 10 km to the larger-scale *bands* exhibiting horizontal wavelengths typically >30 km [*Witt*, 1962; *Fogle and Haurwitz*, 1966]. Later modeling work by *Fritts et al.* [1993] have also suggested that some billows are likely secondary waves originating in nonlinear dissipation ('breaking') of AGW. AGW disturbances mainly originate in the lower atmosphere and propagate upwards, growing in amplitude due to decreasing atmospheric density, eventually becoming unstable and dissipating in the middle atmosphere. The generally accepted theory is that the momentum deposited during this process causes the zonal mean eastward flow in the mesosphere and drives the equatorward and upward residual circulations leading to adiabatic cooling of the mesosphere and the cold summer mesopause.

[4] The relationship existing between AGW associated temperature and dynamical variations and PMCs have been studied from both observations and from microphysical models. *Chandran et al.* [2010] have shown the presence of a longitudinal variability in the occurrence of AGW activity which is anti-correlated to PMC occurrences from observations made by the Cloud Imaging and Particle Size (CIPS) experiment, operating on the AIM satellite [*Russell et al.*, 2009]. Negative correlation between short period AGW activity in the stratosphere and PMC backscatter has been observed from lidar observations at Söndrestrom (67°N) [*Gerrard et al.*, 1998, 2004; *Thayer et al.*, 2003] and Rothera (67.5°S) [*Chu et al.*, 2009] while similar lidar measurements above Kühlungsborn (54°N), Germany [*Gerding et al.*, 2007] ALOMAR (69.3°N), Norway [*Schöch*, 2007] and Davis (68.6°S), Antarctica [*Innis et al.*, 2008] showed no significant correlation. *Chandran et al.* [2010] suggests that the inconsistencies in results from lidar observations made at different locations regarding correlations between NLC backscatter and local AGW activity may result from geographical differences in the background temperatures at PMC altitudes and the amount of local AGW activity.

[5] In this study we present results of numerical simulations of PMC growth in the presence of AGWs of various scales and time periods, from a two dimensional (2D) version of the Community Aerosol and Radiation Model for Atmospheres (CARMA 2D). The purpose of this modeling study is to address the question of whether AGWs can account for the rapid, orbit by orbit change in cloud structure and brightness seen in sequential CIPS images [*Rusch et al.*, 2009]. The CARMA 2D model has been initialized with temperature measurements from Sounding of the Atmosphere using Broadband Emission Radiometry (SABER) instrument on the NASA Thermosphere Ionosphere Mesosphere Energetics and Dynamics (TIMED) satellite and water vapor measurements from the Microwave Limb Sounder (MLS) experiment on board the AURA satellite for the 2008 NH PMC season. We compare the simulated PMC brightness with observations from the CIPS experiment. The paper is laid out as follows: We first describe the CIPS experiment followed by description and initialization of the CARMA 2D model including results from a sensitivity study in sections 2 and 3.1, respectively. This is followed by results from model runs describing in detail the PMC microphysics in the presence of AGWs of variable scales and periods in section 3.1. In section 4 we discuss the results and present our conclusions in section 5.

## 2. Cloud Imaging and Particle Size Experiment (CIPS)

[6] The CIPS instrument [*McClintock et al.*, 2009] consists of four UV nadir imager cameras that image the earth's albedo with a band pass centered at 265 nm and extending from 258 nm to 274 nm (half-power points). The four CIPS cameras have an overlapping field-of-view (FOV) of 120° (along orbit track) × 80° (cross orbit track). The details of the CIPS instruments, camera configuration and first results can be found in *Rusch et al.* [2009]. Orbit 'strips' are made by merging together the individual camera images (level 2). CIPS cameras take an image every 43 s with an exposure time of ∼1 s. On average each CIPS camera takes 26 images per orbit over the sunlit summer polar region. A description of the various CIPS data products is available online from the AIM website at http://aim.hamptonu.edu/library/documentation/instruments/cips/cips_docs.html. For this study we have used the PMC albedo at $\theta = 90$ degree scattering angle ($A_{\lambda=265nm}^{\theta=90°}$) of version 4.20 of the CIPS data. Throughout the manuscript we use $G = 10^{-6}$ sr$^{-1}$ as "unit" [*Baumgarten et al.*, 2012] of the PMC albedo (sometimes also called "brightness") to simplify the text.

### 2.1. PMC Variability in CIPS Orbits

[7] Figure 1 has two sets of consecutive CIPS orbit strips (level 2 data) on July 22nd 2010, which illustrates the growth and sublimation of PMCs in a very short time period between consecutive orbits (∼90 min). In the first set on the left (orbit 17644 and orbit 17645) it can be observed that a bright band of PMC appears just poleward of 80°N between 90°W to 135°W longitude (indicated by the red oval), in orbit 17645 which is absent in the previous orbit (17644). The clouds in this region have increased in brightness by more than $A_{\lambda=265nm}^{\theta=90°} \sim 15$ G from 10 G to 25 G, in a period of 90 min at a rate of ∼10 G/hr. In the orbit strips on the right (orbit 17648 and orbit 17649) a rapid sublimation of existing clouds can be seen between 180°E to 90°E equatorward of 80°N. In the region marked by the red oval there is virtually complete sublimation of the pre-existing PMC to be sub-visual to CIPS and the cloud brightness falls from ∼15 G to <1 G in 90 min. Images of PMC from CIPS constantly show, orbit by orbit change in cloud structure and brightness at a peak rate of ∼15 G/hr over overlapping regions. In fact, CIPS orbits rarely show the same cloud structure persisting in consecutive orbits. This indicates the destruction of existing PMCs, the formation of new PMCs or the rapid growth of sub-visual ice crystals to visible sizes. *Fiedler et al.* [2011], using lidar data have also shown
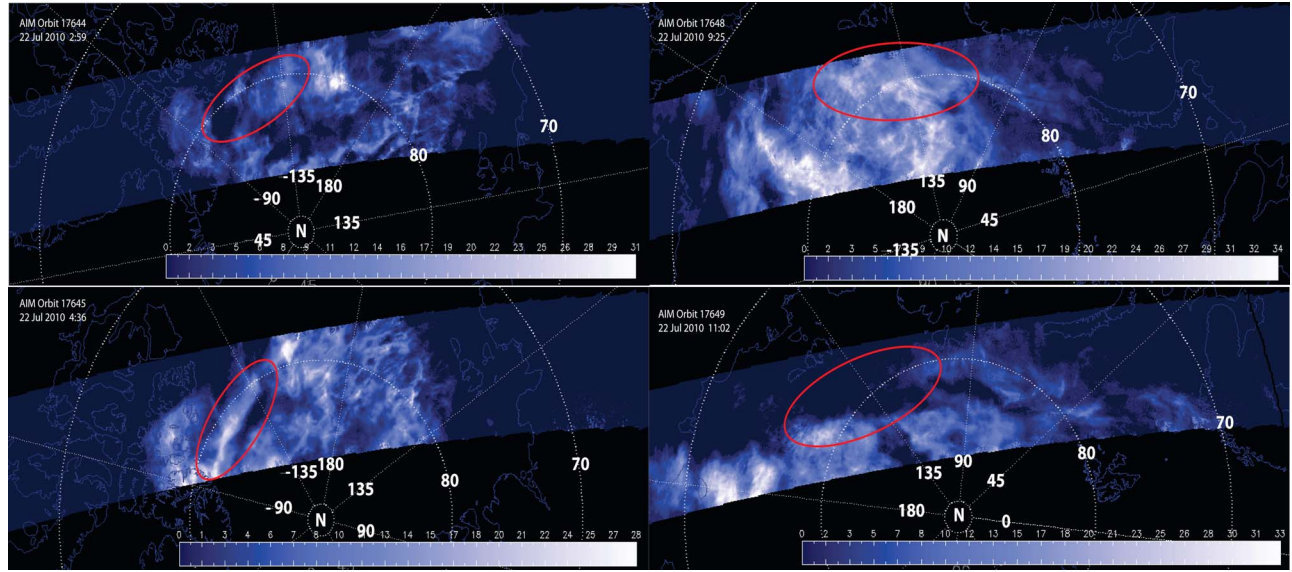
**Figure 1.** Two sets of consecutive orbit strips from CIPS images from July 22nd 2010. (left) PMC growth and (right) PMC sublimation in the regions marked by the red oval.

similar rapid changes in PMC strength over short time periods. Previous modeling studies from *Jensen and Thomas* [1994] and *Rapp et al.* [2002] have indicated a much longer generation time for PMC than the 90 min between CIPS orbits. Another possibility is that the background wind at these altitudes is advecting the PMCs into/out of the observed region. However, to move the clouds into and out of the CIPS FOV would require winds in excess of ~60 m/s (~325 km in 90 min). While instantaneous winds at mesospheric altitudes might exceed 60 m/s due to planetary or gravity waves [*Larsen*, 2002], they are not constantly present in the polar summer mesosphere. *Fiedler et al.* [2011] have reported smaller mean values (44 ms$^{-1}$) for summertime zonal and meridional (−0.5 ms$^{-1}$) winds at PMC altitudes and at 69°N latitude.

[8] The CIPS images also show a wide variation in cloud albedos ($A_{\lambda=265\mathrm{nm}}^{\theta=90^{\circ}}$) ranging from a few G to nearly 80 G. Consistent with previous observations [e.g., *Olivero and Thomas*, 1986] during the cloud season, there is also a significant increase in mean PMC albedos with latitude. The onset of PMCs, which occurs ~20–30 days before summer solstice (hence after referred to as solstice), can be attributed to a pre-solstice decrease in temperature and increases in water vapor concentrations, and the offset of the PMCs can be attributed to warming above the frost point ~60–70 days following solstice [*Hervig et al.*, 2009; *Rong et al.*, 2012].

## 3. The CARMA Model

[9] The Community Aerosol and Radiation Model for Atmospheres (CARMA) has evolved over the past 25 years and various versions have been used to study PMC microphysics [*Turco et al.*, 1982; *Jensen and Thomas*, 1994, *Rapp et al.*, 2002, *Rapp and Thomas*, 2006]. *Turco et al.* [1982] and *Toon et al.* [1989] provide a detailed description of the treatment of ice microphysics in CARMA. *Jensen and*

*Thomas* [1994] first used a 2D version of CARMA to study the effects of AGWs on the formation and evolution of PMCs. The 2D version was later used by *Rapp et al.* [2002] who extended the previous study on AGW/PMC interactions, by including AGW parameters obtained from rocket-borne in situ observations of wind and temperatures during simultaneous NLC observations from lidar.

[10] As the TIMED satellite yaws ~20–23 days after solstice (June 20 in 2008) and thus does not cover an entire PMC season, the results from CARMA runs presented in this study use a mean SABER temperature profile for 20 days after solstice (day of the year 172–192) at 75°N during the 2008 northern hemisphere (NH) PMC season. The water vapor profiles for different latitudes were obtained from measurements from the Microwave Limb Sounder (MLS) experiment on board the AURA satellite for the respective seasons [*Waters et al.*, 2006]. The vertical wind profile with a maximum upward velocity of ~2.8 cm/s at 87 km has been adopted from model simulations with the COMMA/IAP model [*Berger and von Zahn*, 1999] and was previously used in the *Rapp et al.* [2002] CARMA simulation studies. The photolysis rate of water vapor by solar Ly-$\alpha$ and Schumann-Runge irradiance has been parameterized as described in *Jensen and Thomas* [1994]. The computational domain of the model includes 120 vertical levels between 70 and 100 km altitudes. The model has 40 horizontal levels with a usual grid spacing of 15 km, corresponding to a horizontal domain of 600 km. For runs, where an 800 km horizontal wavelength AGW is propagated through the model, the horizontal levels have a grid spacing of 20 km corresponding to a horizontal domain of 800 km to encompass the entire wave. The model has been run with the size distribution and height profile of meteoritic smoke particles from *Hunten et al.* [1980] as well as *Bardeen et al.* [2010]. The differences between the two dust distributions do not produce appreciable changes in brightness of PMCs

for the simulations described in this study. These results are consistent with a recent model study by *Megner* [2011] who showed that PMC properties are remarkably insensitive to the nucleation process. The time step used in the model is 50 s. For the water vapor saturation pressure, the expression from *Marti and Mauersberger* [1993] has been used, following the recommendation by *Rapp and Thomas* [2006].

[11] The CARMA model has been previously run in two ways. A 'cold start' approach by using initial temperatures profiles, representative of the observed summer background conditions, which result in a super-saturated state. Alternatively the model has also been run by starting the model with background temperatures which are warmer, resulting in background conditions being sub-saturated and then progressively cooling the model to produce super-saturated regions where ice nucleation takes place. While *Rapp et al.* [2002] noted that there were no significant differences between the two approaches; *Stevens et al.* [2010] have argued that the clouds grow more steadily when the air starts out sub-saturated and then progressively becomes more saturated, as the model is cooled. *Merkel et al.* [2009] have also noted that 1-D CARMA should not be initiated with supersaturated conditions which led to too many ice particles initially. Their approach was to also start the model with warmer temperature and progressively cool the air. For our current study, we have found that the cold start approach by *Rapp et al.* [2002] by which the model is initialized from a highly supersaturated state, results in rapid nucleation of ice particles, especially at high saturation ratios leading to a rapid depletion of water vapor in the cloud forming region. This results in unrealistically small particle sizes and lower overall albedo ($A_{\lambda=265\mathrm{nm}}^{\theta=90^\circ}$) since the albedo is proportional to the number of particles, N and particle size, r, by the relation, $A_{\lambda=265\mathrm{nm}}^{\theta=90^\circ} \propto N* r^s$, where $s$ is about 3. Scattering cross-sections for particle sizes larger than 50 nm at UV wavelengths increases at a rate significantly smaller than $s = 6$ and more comparable to $s = 3$ [*Rapp and Thomas*, 2006].
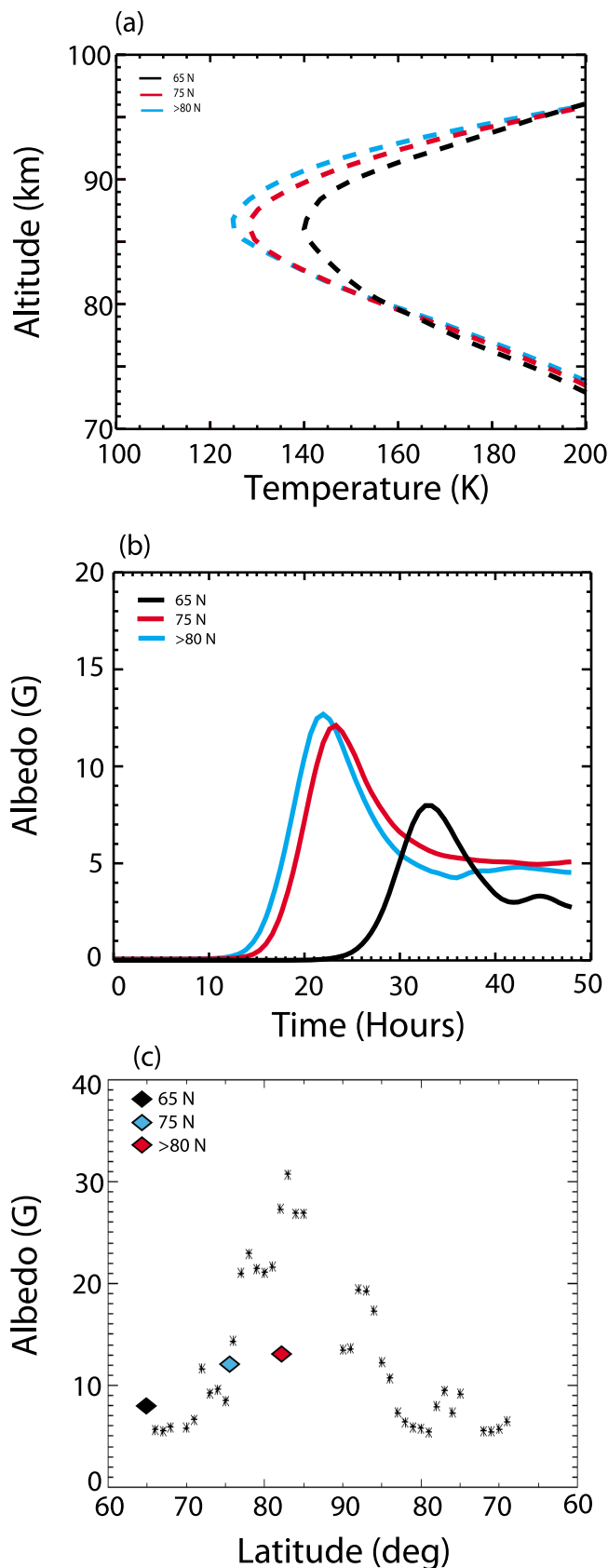
[12] In the presence of large particle numbers and the limited water supply, the particle sizes are too small, resulting in model clouds dimmer than observed. We adopt the warm-start approach in our model simulations as it generally resulted in clouds closer to observed values, as will be shown later. The simulation is started by using initial conditions warmer than the observed mean state of the atmosphere by ∼20 K, with the air being sub-saturated. The atmosphere is then progressively cooled at a rate of 1 K/hr for the first 20 h, consistently throughout the model, to attain the mean state of the atmosphere, after which the temperature is held constant using the prescribed temperature profile.

[13] To test the sensitivity of the model to mean background atmospheric conditions of temperatures and water vapor, we have run the CARMA model with dust and water vapor profiles as described above with no AGWs perturbing the background state and starting the model under warm start conditions. We do not show these results here since the model results with no AGW are similar to those presented in Figure 7 of *Rapp et al.* [2002]. However, our results compare favorably with their results, and therefore consider our model results to be consistent with the earlier work. The formations of PMCs in the CARMA model can be briefly

explained as follows. As the background temperature is lowered and reaches SABER observed values, with minimum temperatures of ∼125 K between 85 and 88 km altitudes, at 20 h into the simulation, the air becomes increasingly saturated and ice nucleation begins to take place on the largest dust particles (>1 nm) in the distribution at altitudes near the mesopause. These ice particles grow bigger as they sediment and more water vapor from the lower altitudes is deposited on the ice nuclei, as they grow and descend. As the simulation proceeds, the water vapor concentration becomes depleted through growth by the increasingly larger and numerous ice particles. The ice particles attain their maximum size before sedimentation and sublimation between ∼81–82 km altitude. As the ice particles sublimate they deposit the water vapor at these altitudes, causing an increased concentration of water vapor at the sublimating altitudes. This 'hydration peak' is now well understood, being reported first by *Summers et al.* [2001]. The ice particles reach their peak size approximately 20–23 h after the commencement of the simulation when background temperatures observed by SABER are reached.

[14] The SABER temperature measurements have shown a negative poleward temperature gradient during the PMC season as predicted by many previous models. Previous CARMA studies from *Lübken et al.* [2007] have shown the sensitivity of the CARMA model to background temperatures. We have run the model using mean temperatures at 65°N, 75°N and poleward of 80°N from SABER for the 2008 NH PMC season, shown in Figure 2a. The summer mesopause lies between 86 and 88 km at the high latitudes as seen from SABER measurements [*Russell et al.*, 2010]. The SABER mesopause temperatures are ∼2–3 km lower than the mesopause temperatures observed from lidar measurements from fixed locations [*Lübken and Müllemann*, 2003]. The mean SABER temperature decreases by almost ∼8 K from 65°N to 80°N. The maximum albedo ($A_{\lambda=265\mathrm{nm}}^{\theta=90^\circ}$) as shown in Figure 2b increases from 8 G to ∼13 G, from 65°N to 80°N. In both cases, the maximum albedo corresponds to when the biggest ice particles are formed, followed by albedo decreases to 3 G and 5 G, respectively. However, the differences between 75°N and 80°N are considerably smaller which is indicative of the smaller temperature difference as well as the reduced response to lower temperatures. Even running the CARMA model with still lower temperature than SABER observed values above 80°N also fails to produce brighter PMCs. This is caused by the depletion of water vapor between 81 and 87 km. Figure 2c shows the latitudinal variation in mean PMC brightness (binned in 2 degree latitude bins) from 60 N to the pole (ascending node of orbit) and from the pole to 60 N (descending node of orbit) from a CIPS orbit compared with maximum brightness observed from CARMA model runs. We observe that CARMA reproduces the general increase in albedo with latitude as observed by CIPS, but the overall PMC albedo from CARMA is significantly lower (by almost a factor of 2.5) than the mean PMC values observed from CIPS.

[15] Running the CARMA model with increased background water vapor concentrations result in overall brighter PMCs. The sensitivity of the model to background water vapor concentrations is given in Figure 19 of *Rapp and*

**Figure 2.** (a) Mean SABER temperature at 65°, 75° and >80°N during 2008 NH PMC season. (b) Corresponding PMC albedos from CARMA. (c) Comparison of latitudinal dependence of mean albedo in two degree latitude bins from CIPS observations for a single orbit on July 14, 2008 and from CARMA using mean temperatures at 65°, 75° and >80°N.

*Thomas* [2006]. Increasing the background water vapor concentration by a factor of 1.5 increases the PMC albedo by a factor of 2. We have also tested the sensitivity of the CARMA model to water vapor concentrations by running the model without dehydration, i.e., by turning off the freeze drying and redistribution of water in the model. This can be considered as instantaneous replenishment of water as ice particles grow. Once the temperature is sufficiently low, the PMC brightness is controlled primarily by the amount of water vapor available for nucleation and for ice particle growth. Once the air has been desiccated, the ice particles cannot grow any bigger and the PMC brightness achieves a limit determined by the available water content. Above 80°N, extremely bright PMCs (albedo higher than 150 G) are produced by the model and the brightness values are changed only when the dust distribution is altered. This indicates that almost all the condensation nuclei participate in the nucleation process. This extreme case represents an upper limit of how fast the PMCs can grow in the presence of instant replenishment of water vapor, when sufficiently low temperatures are present. However, at 65°N even in the presence of instant water vapor replenishment, the, PMC albedos are almost the same as that at 65°N with a normal water vapor profile. This is explained by the fact that at these relatively high temperatures, the water mass tied up as ice is small compared to the vapor content, so that freeze-drying is modest. These results agree well with results from *Rapp and Thomas* [2006] and *Lübken et al.* [2007]. They found that generally when the temperature is lowered and the water vapor concentration is increased the albedo increases. The exception is when the mesopause temperature gets too low, in which case too many ice particles get nucleated and the water vapor is rapidly depleted resulting in smaller ice particles and lower albedo.

### 3.1. CARMA Results From AGW Runs

[16] Here, we discuss results from model simulations of ice growth and albedo perturbations due to AGWs. Figure 3 shows the PMC growth in the presence of an AGW of 600 km horizontal wavelength ($\lambda_x$), 6 km vertical wavelength ($\lambda_z$) and wave period of 615 min at a mean background temperature at 75°N. It is a six panel figure which shows the temporal evolution of (a) temperature, (b) water vapor (c) ice saturation ratio (d) ice concentration (e) mean radius versus time along the x axis at 250 km in the horizontal domain and (f) PMC albedo $A_{\lambda=265nm}^{\theta=90°}$ along the horizontal grid with time. In previous CARMA modeling studies of PMCs, *Jensen and Thomas* [1994] used vertical wavelengths of 6.9 km for a 100 km and 1000 km horizontal wavelength AGWs, while more recently *Rapp et al.* [2002] presented results of PMC growth in the presence of a 6 km vertical wavelength and 595 km horizontal wavelength AGW. In this study, by varying the horizontal wavelength
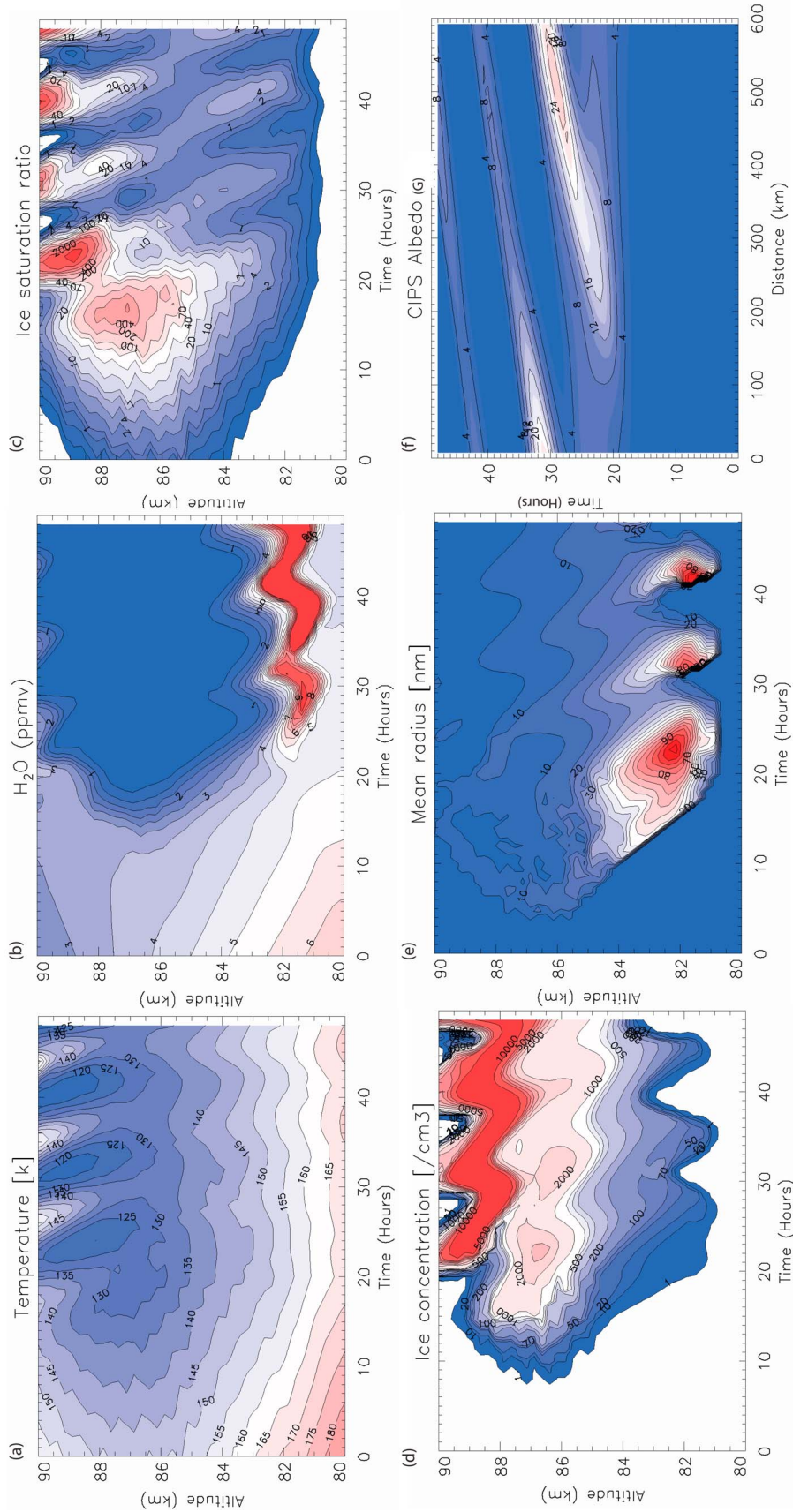
**Figure 3.** CARMA 2D simulation showing growth of ice layer in the presence of an AGW of $\lambda_x = 600$ km, $\lambda_z = 6$ km, and period of 615 min, at 75°N. Figure shows the temporal evolution of (a) temperature, (b) ice saturation ratio, (c) water vapor, (d) ice concentration, (e) mean radius, and (f) change in PMC albedo at 265 nm as a function of horizontal location.

and time periods of the gravity waves in accordance with the dispersion relation for non-inertial gravity waves [*Fritts and Alexander*, 2003], $\hat{\omega}^2 = \dfrac{N^2(k^2 + l^2)}{k^2 + l^2 + m^2} = \dfrac{N^2 k_h^2}{k_h^2 + m^2}$ where $\hat{\omega}$ is the intrinsic frequency, where $N$ (s$^{-1}$) is the Brunt-Väisälä frequency (=0.017) and $k$, $l$, $m$ are the wave number vectors, while keeping the vertical wavelength constant, we quantify the influence of different types of AGWs. We classify AGWs with periods <5 h and horizontal wavelength ($\lambda_x$) <300 km as short period, short horizontal wavelength gravity waves and AGWs with periods >5 h and $\lambda_x$ > 300 km as long period, long horizontal wavelength gravity waves. We refer to the AGWs as such in this paper and is not be confused with other classification schemes used for AGWs.

[17] Following *Jensen and Thomas* [1994], the vertical and horizontal winds are defined as follows

$$w = \bar{w} + \tilde{w}_0 . \cos(k_x x + k_z z - \omega t) \tag{1}$$

$$u = -\tilde{w}_0 . \frac{k_z}{k_x} . \cos(k_x x + k_z z - \omega t) \tag{2}$$

where, $w$ is the vertical wind, $u$ is the horizontal wind, $k_x$ is the horizontal wave number, $k_z$ is the vertical wave number, $\omega$ is the frequency and $t$ is the time. $\tilde{w}_0 = \dfrac{\Delta t}{T_0(70\,\mathrm{km})} . \dfrac{g\omega}{N^2} . \exp\left(\dfrac{z - 70\,\mathrm{km}}{2.7\,\mathrm{km}}\right)$, Above altitudes of 92 km $\tilde{w}_0$ is additionally multiplied by a factor $\exp\left(-\dfrac{(z - 92\,\mathrm{km})^2}{(2.5\,\mathrm{km})^2}\right)$, to avoid unreasonably large AGW amplitudes. $k_z$ is negative for downward phase propagation. $\bar{w}$ is the background vertical wind. $\Delta T = 2$ K and $T_0(70$ km$)$ is the undisturbed background temperature at 70 km altitude. In the model an air parcel that is advected out of the eastern boundary of the computational domain is advected into the domain again from the western boundary. The AGW is turned on in the model after 12 h. The wave amplitude is gradually built up to maximum values over a period of 12 h until its final value of $\tilde{w}_0$ is reached. This is done similar to the warm start approach used for the mean background conditions.

[18] The introduction of a long period, large horizontal wavelength gravity wave produces significant perturbations in all parameters in Figure 3. Figure 3a shows the model realization of the AGW modified temperature, it is apparent that in the presence of the AGW the temperatures are lower during the cold phase of the wave, reaching even below 120 K at the mesopause. The modeled temperature perturbations extend upward to 90 km. Figure 3b is a plot of the water vapor mixing ratio. As the model domain is cooled, the ice concentration is increased, and the growing ice particles descend and deplete the water vapor in the domain between 81 and 89 km. The particles attain maximum size before they sublimate around 81 km and deposit water vapor as the ice sublimates. Thus the ice particles play a major role in redistributing the water vapor profile by transporting the water vapor from the altitude range of 82 to 89 km down to below 82 km. The water vapor concentration is enhanced below 82 km from its background value of 4 ppmv to a peak of 9–10 ppmv. Isoline of water vapor at 0.5 ppmv shows the

freeze-dried region. The long period AGW induces vertical wind (of ∼7–12 cms$^{-1}$ at 80–82 km), which acts for significant periods like a pump, transporting upward the water vapor by about 2–3 km in altitudes. The water is transported into an otherwise freeze-dried region in a non-AGW situation. This serves as an additional water source for further growth of descending ice particles, enabling them to grow larger than in the non-AGW run. The upward velocity from the AGW induced vertical wind perturbation also slows down the descent of the ice particles enabling them to survive longer and grow to larger particles. The presence of larger particles results in higher PMC albedo. The maximum albedo during this run is ∼24 G while for the no-AGW case the maximum PMC albedo was ∼12 G. For AGWs of larger horizontal wavelength and longer periods the maximum albedo is even higher.

[19] Figure 3c is a plot of the ice saturation ratio and Figure 3d of ice concentration. It can be seen from these figures that the increase in ice saturation ratio and ice concentrations closely follows the cold phase of the wave. The ice concentration plot shows significantly higher numbers of ice particles nucleating at higher altitudes during the cold phase of the wave. Figure 3e shows the mean radius of ice particles. Compared to no-AGW runs, there are two additional secondary peaks of large particles which form ∼32 and 42 h into the simulation. These correspond to the cold phase of the wave which has a period of ∼10 h. In the absence of AGW, the model produces one peak at near 23 h. The albedo peak at 32 h and 42 h occur in addition to the peak at 23 h. These secondary peaks in particle sizes are driven by the AGW making available additional water vapor for descending ice particles. There is therefore a higher number of large particles in this case compared to no-AGW model run. Figure 3f is a plot of PMC albedo $A_{\lambda=265\mathrm{nm}}^{\theta=90°}$ along the horizontal grid with time. As the albedo is a function of both particle size and ice concentration, the brightest clouds are formed ∼30 h into the simulation, when there is the highest concentration of large particles.

[20] We now compare the results of a number of runs with different AGW characteristics. Figure 4a shows the albedo and Figure 4b shows ice water content (vertically integrated) variations in the presence of short period ($\lambda_x$ = 100 km, period = 102 min and $\lambda_x$ = 300 km, period = 308 min) and long period AGWs ($\lambda_x$ = 600 km, period = 615 min and $\lambda_x$ = 800 km, period = 775 min), at a fixed location at 250 km in the horizontal domain in the model. All the waves have a vertical wavelength of 6 km. From these figures, it can be seen that the effect of short period AGW are to produce small (a few G) perturbations of $A_{\lambda=265\mathrm{nm}}^{\theta=90°}$ about the no AGW case while the long period AGW produce significant increases in albedo on the order of two to three times the maximum value observed when the AGW is not present. The long period AGWs also cause rapid variation in PMC brightness at a peak rate of ∼6 G/hour. This translates to peak growth rates of ∼9 G/ 90 min. The reason for this is the upward (and downward) vertical velocity perturbations acting for long durations. The wave transports the water from altitudes below 82 km to ∼2 km above. The sedimenting ice particles use up this extra water to grow to bigger particles, creating brighter PMCs. The lifetimes of these ice particles are very short as they quickly sublimate, when they reach the lower altitudes where the air becomes
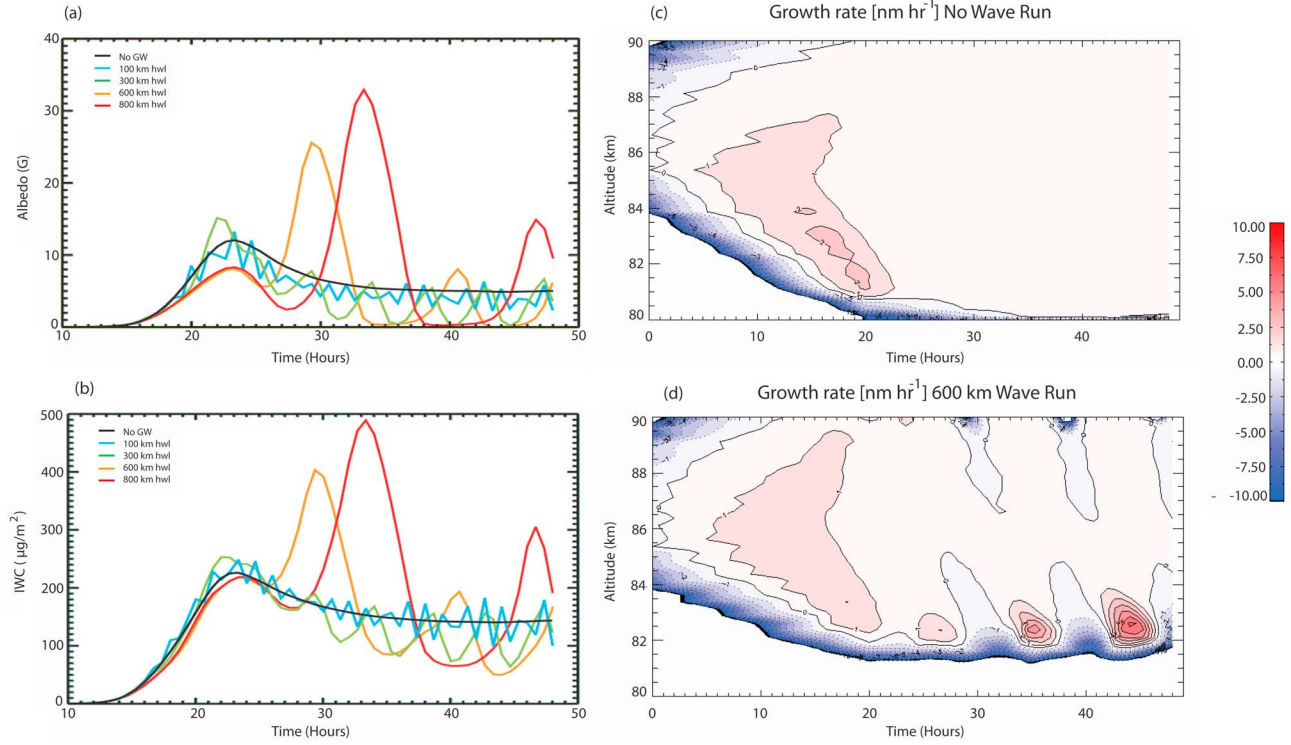
**Figure 4.** (a) PMC albedo and (b) ice water content variation in the presence of AGW of different scales. (c) CARMA 2D growth rates in the model for no AGW simulation and (d) $\lambda_x$ = 600 km AGW simulation.

warm and sub-saturated. Hence the growth time is only slightly longer than the time taken for destruction of the PMCs. Figures 4c and 4d show the growth rates in the model for the no-AGW model run and 600 km AGW run respectively. The blue values (dotted lines) represent negative growth rates or sublimation. From the growth rate plots it can be seen that in the long-period AGW runs, the secondary and tertiary peaks in albedo after ~25 h into the simulation

are driven by enhanced growth rates due to the upwelling of water due to the AGW, and the upward directed vertical wind which keeps growing ice particles for a longer time in the super-saturated region.

[21] Figure 5 is a plot of the domain averaged PMC albedo for short-period and long-period AGW cases compared to the PMC albedos for a no-AGW run. It can be seen that when the albedo is averaged over the whole domain (both x
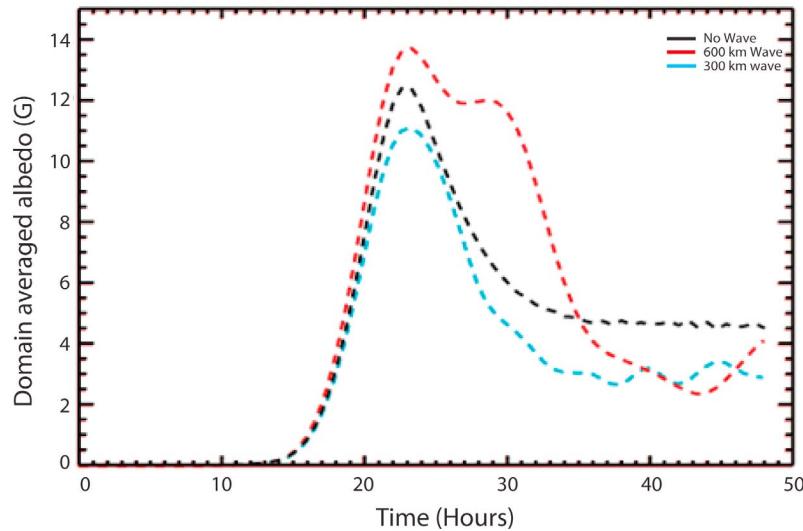


**Figure 5.** Domain averaged PMC albedo for no-AGW and short period (300 km horizontal wavelength) and long period (600 km horizontal wavelength) AGW.
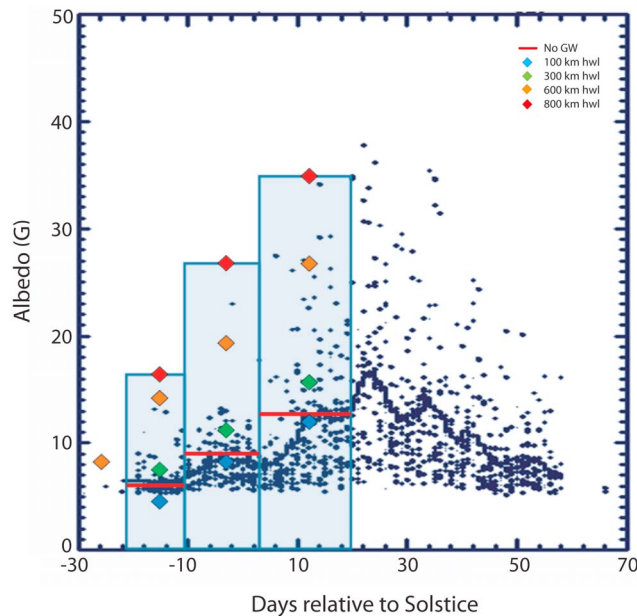
**Figure 6.** Plot of the seasonal variation in daily mean PMC albedo as seen by CIPS between 75–80°N and ranges of albedos produced from CARMA for the 2008 NH PMC season.

and z directions) of the model, the results are not very different from the no-AGW case. The PMC albedo for a short-period, small horizontal wavelength AGW is always less than the PMC albedo for the non-AGW (reference) case, as shown earlier by *Jensen and Thomas* [1994]. For a longer period, larger wavelength AGW, while initially the PMC albedos are higher than in the reference case, the albedos fall below the reference case after about 36 h into the simulation. So while the long-period AGW can result in brighter PMC temporarily, they tend to reduce the PMC brightness over a longer period of time. So both the short period and long period AGW ultimately cause diminished PMC brightness as suggested by *Rapp et al.* [2002].

[22] Figure 6 shows the seasonal variation in mean orbit by orbit PMC albedo as seen by CIPS between 75–80°N and the ranges of albedos simulated by CARMA for the 2008 NH PMC season. The solid black line indicates the daily mean PMC values. The abscissa indicates days relative to solstice. The period from the start of the PMC season in late May to ∼23 days after solstice (June 20 in 2008), during which SABER temperature data is available, has been binned into three periods as shown in the figure. The model was run by taking the SABER mean temperatures between 75–80°N latitudes as the background temperature for these periods. The solid red line in the plot is the peak PMC brightness value predicted by CARMA with no-AGW perturbing the background atmosphere. The diamonds are color coded for peak albedos produced in the respective AGW runs. The blue shaded regions represent the ranges of PMC albedo produced by CARMA in both AGW and no-AGW runs. At any instant during the model run, the cloud brightness could be anywhere within the blue shaded region depending on the location within the horizontal domain of the model and the time of progression of the run. As shown

in Figure 5a, short period waves (green and blue diamonds) produce minor variations in the albedo about the no-AGW PMC albedo, while the larger horizontal scale (longer period) AGW (red and orange diamonds) produce significant increases in the PMC albedo. The mean daily PMC values observed by CIPS lie close to the maximum PMC brightness produced by CARMA for a no-AGW simulation (indicated by the red line). The whole range of mean PMC brightness for CIPS orbits also lie within the range of PMC brightness produced by CARMA using AGWs. However, it should be noted that maximum cloud brightness for individual PMCs can be up to a factor of 4 more than the maximum cloud brightness produced by CARMA under no-AGW conditions and up to a factor of 2 more than the maximum cloud brightness produced by CARMA using AGWs.

## 4. Discussion

[23] As discussed in the introduction, CIPS images have shown rapidly varying PMC brightness and structures between orbits spaced ∼90 min apart. *Rapp et al.* [2002] using a 'cold-start' approach for the CARMA model with both no-AGW and AGW simulations, have reported growth times of between 5 and 10 h for PMCs to become visible when growing from 2 nm (the critical size of a dust particle to produce nucleation). Our current simulations also indicate ∼15–20 h for PMCs to become visible when growing from this small size and using the 'warm-start' approach. Therefore the rapid variation in brightness seen 90 min apart cannot be caused by nucleating and growing new PMCs. As can be seen from the result of the different initialization procedures used by *Rapp et al.* [2002] and this manuscript, the question about the time since nucleating the particles goes beyond the capabilities of the CARMA model in the present set up. We considered the possibility that the rapid change in PMC albedo is explained by the advection of PMCs by the background winds. As the CIPS field of view (FOV) is limited to about 1000 km × several 1000 km the clouds could have advected in or out of the FOV. However, to move the clouds into and out of the CIPS FOV would require winds in excess of ∼60 m/s (∼325 km in 90 min). While winds of this magnitude have been observed at PMC altitudes, they are quite infrequent [e.g., *Fiedler et al.*, 2011] while the changes in PMC albedo are a very common occurrence.

[24] From our results in the previous section, we argue that the rapid changes observed in PMC albedos from CIPS images are driven by the growth of sub-visual ice particles (r < 30 nm) to visual particles (r > 30 nm). In the presence of long period gravity waves, the upward vertical winds associated with the gravity wave can last for long periods of time. This acts as a pump to provide significant amounts of water vapor to colder regions between 81 and 84 km providing 'extra' water vapor to descending ice particles. The gravity wave enhanced upward vertical wind also slows down the descending ice particles and enables them to stay for longer in the super saturated region. This allows the ice particles to grow rapidly increasing the PMC albedo significantly. In the CARMA model, once PMC growth has occurred and the simulation has been run for ∼20 h, there is a water-poor region between 82–89 km and a water-rich reservoir below

82 km due to the sublimating ice particles. Because of the-water depletion in the model, the PMC brightness is controlled by the size to which ice particles can grow. In the no-AGW model run, after 20 to 25 h into the simulation, there are a large number of particles with a size of ~40 nm. However, in the presence of long period AGWs, there is a secondary and tertiary peak in particle sizes at 32 h and 42 h into the simulation driven by the upwelling of water and the upward vertical wind driven by AGWs. This enables the ice particles with sizes between 20 to 40 nm to grow to as much as about 100 nm. The PMC albedo thus increases at the rate of ~6 G / hour in the presence of long period AGWs. In effect, the waves act like a pump, transporting water upward from unsaturated water-rich regions to the colder water-poor regions where smaller (sub-visual) ice particles are pre-existing. The pump acts on the water vapor more effectively than on the ice particles, since they are influenced by downward sedimentation. The surge of water allows the particles to grow rapidly, and thus their brightness increases rapidly in the upward wind phase. In the opposite phase of the wave, the pump transports water (and particles) downward, causing a negative growth rate and lower brightness. Such effects of AGW on trace gas transport have been investigated on global scales recently by *Grygalashvyly et al.* [2011]. While AGWs with short horizontal wavelengths and short period induce higher vertical velocities than large period large horizontal wavelength AGWs, they do not last long enough for this process to significantly change PMC brightness. The decrease in brightness can be easily explained by the sublimation of ice particles as they descend and encounter warm temperatures, which has been shown by previous modeling studies. The lifetime of these ice particles are very short as the descent rates of ice particles are also accelerated by the AGW driven downward vertical velocities in the next phase of the wave. The downward vertical velocity transports the ice particles faster to the lower altitudes and sublimates the ice particles faster. This explains the accelerated sublimation rates during the downward phase of the wave that can be seen in the growth rate plot (Figures 4c and 4d).

[25] The CARMA 2D model with AGWs can thus produce peak PMC brightness changes at the rate of ~10 G/90 min. The PMC brightness changes in Figure 1 occur at a rate of ~15 G/90 min. Peak brightness changes in CIPS observed PMCs are between 15–20 G/ 90 min. When analyzing single clouds (not daily mean values given in Figure 6) we find PMC albedo in excess of 70 G. It is worth noting that even in the presence of long period AGWs, the maximum PMC albedo simulated by the CARMA model is still less than the brightest PMC observed by CIPS by almost a factor of two. Lidar observations as well as ground based and spaced images of PMCs almost always show the presence of waves of multiple scales [*Baumgarten et al.*, 2012]. Hence the no-AGW case is most probably unrealistic and the PMC brightness is modulated by either short or long period waves or a combination of both.

[26] A short period AGW which has high vertical velocities associated with it, existing in the presence of a large scale large wavelength long period AGW can conceivably transport water to altitudes as high as 85 to 86 km and result in the creation of large ice particles and brighter PMCs. To be more realistic, the CARMA model needs to be run with a combination of short and long period AGWs. Figure 7 is a composite of PMC brightness, $A_{\lambda=265nm}^{\theta=90°}$ made from a no-AGW run and a short period AGW ($\lambda_x = 100$ km, period = 102 min) and a long period ($\lambda_x = 800$ km, period = 775 min) AGW model run, at each vertical grid point. While the PMC brightness between 81 and 82 km is controlled mostly by the short period AGW, the long period AGW controls the PMC brightness at altitudes between 82 and 84 km causing the brightness peaks at hour 27 and at hour 44. A line plot of the PMC brightness at a fixed location is similar to the line plot of albedo for the 800 km wave as shown in Figure 4a but with fluctuation in albedo caused by the shorter scale wave superimposed on it.

## 5. Conclusion

[27] By modeling the growth of Polar Mesospheric Clouds (PMC) in the presence of atmospheric gravity waves (AGW) of various scales, we are able to quantify the effects of AGW on PMC brightness. These simulations permit an understanding of the observed rapid variability in PMC brightness from the CIPS experiment on board the AIM spacecraft. In this study we have used AGW with horizontal scales varying from 100 to 800 km. The long-period (>5 h) large horizontal wavelength AGWs produce the largest enhancements in PMC brightness, while short period (<5 h) AGWs tend to cause oscillations in PMC albedos about the no-wave PMC albedos. Results from model runs with AGW less than 100 km horizontal wavelength are not presented since the net effect of these waves are to produce fluctuations in PMC brightness about the no-wave model run similar to the 100 km AGW run. CARMA 2D model simulations with AGWs significantly enhance the PMC brightness change rate, but are still less than the maximum CIPS observed rate of brightness change.

[28] While the long period AGW can result in brighter PMC temporarily, they tend to reduce the overall PMC brightness over a longer period of time. So both the short period and long period AGW ultimately cause dimmer PMCs. This agrees with CIPS observations of a negative correlation between regions of high AGW activity and PMC brightness over the whole season. From the analysis of PMC structures from *Carbary et al.* [2000] it can be seen that there is a higher percentage of shorter horizontal wavelength waves (<400 km) than larger horizontal wavelength waves. As discussed previously the effect of short period AGW is to produce perturbations in albedo about the no-AGW case. In this context the majority of CIPS observations can be explained by the presence of the more numerous short-period waves with smaller horizontal wavelengths. We suggest that the brightest PMCs are caused by the very large horizontal wavelength, large period waves (>6 h), which constitute a smaller fraction of the AGW spectrum. As shown in Figure 6, both the trends in the seasonal variation in mean daily PMC albedo and the range of mean PMC albedos from CIPS orbits is reproduced by CARMA using a combination of short and long period AGWs. However, the CARMA 2D model cannot reproduce the brightest individual PMC observed by CIPS (almost a factor of 2 more than the brightest CARMA modeled PMCs with AGWs).
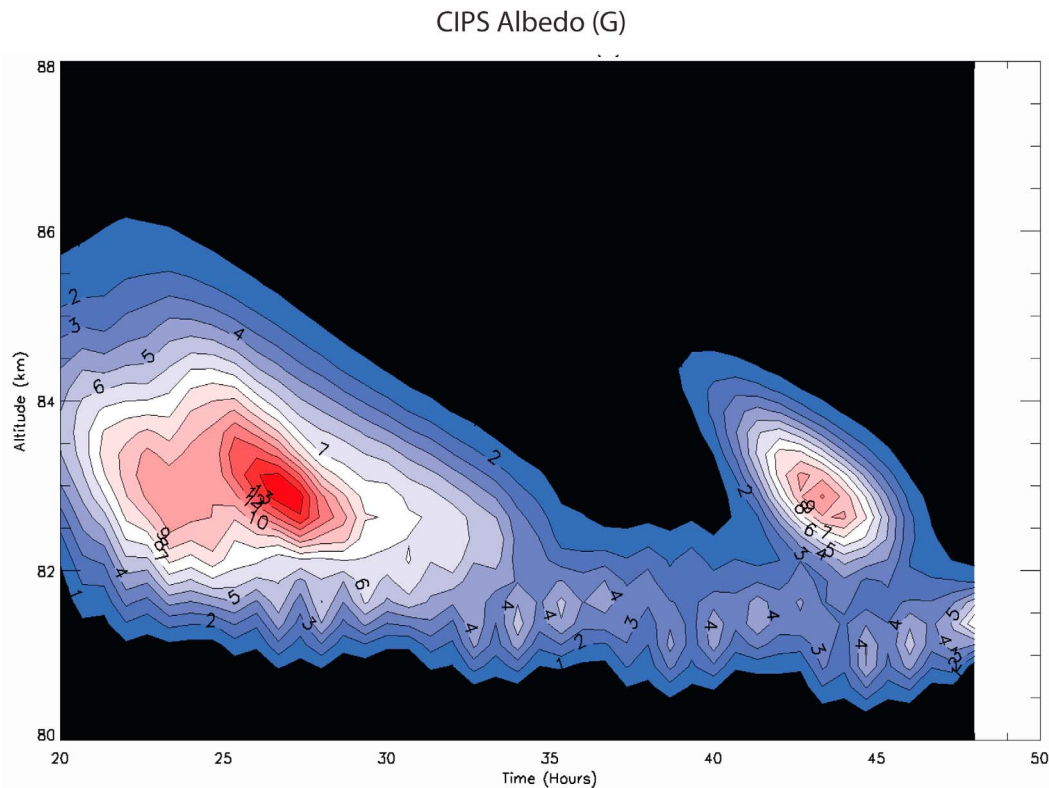
**Figure 7.** A composite of PMC brightness made from PMC brightness from a no-AGW run, a short period AGW ($\lambda_x = 100$ km) and a long period ($\lambda_x = 800$ km) AGW model run.

The CARMA 2D model results with AGW simulations suggest that the rapid orbit by orbit changes in PMC brightness may in part be driven by large horizontal wavelength, long period AGWs. *Chandran et al.* [2010] have shown from CIPS observations, that there is a longitudinal variation in AGW activity and a corresponding negative correlation with PMC occurrence frequency and brightness. However, that study was done for AGWs of horizontal wavelength less than 300 km. To test the hypothesis of the brighter PMCs being driven by large period, large horizontal wavelength AGWs, an appropriate test would be to extend that study to isolate and correlate larger horizontal wavelength waves and correlate the longitudinal variability with the observed longitudinal variability for bright PMCs.

## References

Bardeen, C. G., O. B. Toon, E. J. Jensen, M. E. Hervig, C. E. Randall, S. Benze, D. R. Marsh, and A. Merkel (2010), Numerical simulations of the three-dimensional distribution of polar mesospheric clouds and comparisons with Cloud Imaging and Particle Size (CIPS) experiment and the Solar Occultation For Ice Experiment (SOFIE) observations, *J. Geophys. Res.*, *115*, D10204, doi:10.1029/2009JD012451.

Baumgarten, G., A. Chandran, J. Fiedler, P. Hoffmann, N. Kaifler, J. Lumpe, A. Merkel, C. E. Randall, D. Rusch, and G. Thomas (2012),

On the horizontal and temporal structure of noctilucent clouds as observed by satellite and lidar at ALOMAR (69N), *Geophys. Res. Lett.*, *39*, L01803, doi:10.1029/2011GL049935.

Berger, U., and U. von Zahn (1999), The two-level structure of the mesopause: A model study, *J. Geophys. Res.*, *104*(D18), 22,083–22,093, doi:10.1029/1999JD900389.

Carbary, J. F., D. Morrison, and G. J. Romick (2000), Transpolar structure of polar mesospheric clouds, *J. Geophys. Res.*, *105*(D20), 24,763–24,769, doi:10.1029/2000JD900397.

Chandran, A., D. W. Rusch, S. W. Merkel, S. E. Palo, G. E. Thomas, M. J. Taylor, S. M. Bailey, and J. M. Russell III (2010), Polar mesospheric cloud structures observed from the cloud imaging and particle size experiment on the Aeronomy of Ice in the Mesosphere spacecraft: Atmospheric gravity waves as drivers for longitudinal variability in polar mesospheric cloud occurrence, *J. Geophys. Res.*, *115*, D13102, doi:10.1029/2009JD013185.

Chu, X., C. Yamashita, P. J. Espy, G. J. Nott, E. J. Jensen, H.-L. Liu, W. Huang, and J. P. Thayer (2009), Responses of polar mesospheric cloud brightness to stratospheric gravity waves at the South Pole and Rothera, Antarctica, *J. Atmos. Sol. Terr. Phys.*, *71*(3–4), 434–445, doi:10.1016/j.jastp.2008.10.002.

Fiedler, J., G. Baumgarten, U. Berger, P. Hoffmann, N. Kaifler, and F. J. Lübken (2011), NLC and the background atmosphere above ALOMAR, *Atmos. Chem. Phys.*, *11*, 5701–5717, doi:10.5194/acp-11-5701-2011.

Fogle, B., and B. Haurwitz (1966), Noctilucent clouds, *Space Sci. Rev.*, *6*(3), 279–340, doi:10.1007/BF00173768.

Fritts, D. C., and M. J. Alexander (2003), Gravity wave dynamics and effects in the middle atmosphere, *Rev. Geophys.*, *41*(1), 1003, doi:10.1029/2001RG000106.

Fritts, D. C., J. R. Isler, and G. E. Thomas (1993), Wave breaking signatures in noctilucent clouds, *Geophys. Res. Lett.*, *20*(19), 2039–2042, doi:10.1029/93GL01982.

Garcia, R. R., and S. Solomon (1985), The effect of breaking gravity waves on the dynamics and chemical composition of the mesosphere and lower thermosphere, *J. Geophys. Res.*, *90*(D2), 3850–3868, doi:10.1029/JD090iD02p03850.

Gerding, M., J. Höffner, M. Rauthe, W. Singer, M. Zecha, and F.-J. Lübken (2007), Simultaneous observation of noctilucent clouds, mesospheric

summer echoes, and temperature at a midlatitude station (54°N), *J. Geophys. Res.*, *112*, D12111, doi:10.1029/2006JD008135.

Gerrard, A. J., T. J. Kane, and J. P. Thayer (1998), Noctilucent clouds and wave dynamics: Observations at Sondrestrom, Greenland, *Geophys. Res. Lett.*, *25*(15), 2817–2820, doi:10.1029/98GL02107.

Gerrard, A. J., T. J. Kane, S. D. Eckermann, and J. P. Thayer (2004), Gravity waves and mesospheric clouds in the summer middle atmosphere: A comparison of lidar measurements and ray modeling of gravity waves over Sondrestrom, Greenland, *J. Geophys. Res.*, *109*, D10103, doi:10.1029/2002JD002783.

Grygalashvyly, M., E. Becker, and G. R. Sonnemann (2011), Wave mixing effects on minor chemical constituents in the MLT region: Results from a global CTM driven by high-resolution dynamics, *J. Geophys. Res.*, *116*, D18302, doi:10.1029/2010JD015518.

Hervig, M. E., L. L. Gordley, M. H. Stevens, J. M. Russell, S. M. Bailey, and G. Baumgarten (2009), Interpretation of SOFIE PMC measurements: Cloud identification and derivation of mass density, particle shape, and particle size, *J. Atmos. Sol. Terr. Phys.*, *71*, 316–330, doi:10.1016/j.jastp.2008.07.009.

Hines, C. O. (1968), A possible source of waves in noctilucent clouds, in *Space Research IX*, edited by P. A. Smith et al., pp. 170–174, COSPAR, Tokyo.

Holton, J. R. (1983), The influence of gravity wave breaking on the general circulation of the middle atmosphere, *J. Atmos. Sci.*, *40*, 2497–2507.

Hunten, D. M., R. P. Turco, and O. B. Toon (1980), Smoke and dust particles of meteoric origin in the mesosphere and stratosphere, *J. Atmos. Sci.*, *37*, 1342–1357.

Innis, J., A. R. Klekociuk, R. J. Morris, A. Cunningham, A. Graham, and D. J. Murphy (2008), A study of the relationship between stratospheric gravity waves and polar mesospheric clouds at Davis, Antarctica, *J. Geophys. Res.*, *113*, D14102, doi:10.1029/2007JD009031.

Jensen, E. J., and G. E. Thomas (1994), Numerical simulations of the effects of gravity waves on noctilucent clouds, *J. Geophys. Res.*, *99*(D2), 3421–3430, doi:10.1029/93JD01736.

Larsen, M. F. (2002), Winds and shears in the mesosphere and lower thermosphere: Results from four decades of chemical release wind measurements, *J. Geophys. Res.*, *107*(A8), 1215, doi:10.1029/2001JA000218.

Leslie, R. J. (1885), Sky glows, *Nature*, *32*, 245, doi:10.1038/032245a0.

Lübken, F.-J. (1999), Thermal structure of the Arctic summer mesosphere, *J. Geophys. Res.*, *104*(D8), 9135–9149.

Lübken, F.-J., and A. Müllemann (2003), First in situ temperature measurements in the summer mesosphere at very high latitudes (78°N), *J. Geophys. Res.*, *108*(D8), 8448, doi:10.1029/2002JD002414.

Lübken, F.-J., M. Rapp, and I. Strelnikova (2007), The sensitivity of mesospheric ice layers to atmospheric background temperatures and water vapor, *Adv. Space Res.*, *40*, 794–801, doi:10.1016/j.asr.2007.01.014.

Marti, J., and K. Mauersberger (1993), A survey and new measurements of ice vapor pressure at temperatures between 170 and 250 K, *Geophys. Res. Lett.*, *20*, 363–366, doi:10.1029/93GL00105.

McClintock, W. E., D. W. Rusch, G. E. Thomas, A. W. Merkel, M. R. Lankton, V. A. Drake, M. S. Bailey, and J. M. Russell III (2009), The cloud imaging and particle size experiment on the aeronomy of ice in the mesosphere mission: Instrument concept, design, calibration and on-orbit performance, *J. Atmos. Sol. Terr. Phys.*, *71*(3–4), 340–355, doi:10.1016/j.jastp.2008.10.011.

Megner, L. (2011), Minimal impact of condensation nuclei characteristics on observable Mesospheric ice properties, *J. Atmos. Sol. Terr. Phys.*, *73*(14–15), 2184–2191, doi:10.1016/j.jastp.2010.08.006.

Merkel, A. W., D. W. Rusch, S. E. Palo, J. M. Russell III, and S. M. Bailey (2009), Mesospheric planetary wave effects on global PMC variability inferred from AIM–CIPS and TIMED–SABER for the northern summer 2007 PMC season, *J. Atmos. Sol. Terr. Phys.*, *71*(3–4), 381–391, doi:10.1016/j.jastp.2008.12.001.

Olivero, J. J., and G. E. Thomas (1986), Climatology of polar mesospheric clouds, *J. Atmos. Sci.*, *43*(12), 1263–1274.

Rapp, M., and G. E. Thomas (2006), Modeling the microphysics of mesospheric ice particles: Assessment of current capabilities and basic sensitivities, *J. Atmos. Sol. Terr. Phys.*, *68*, 715–744, doi:10.1016/j.jastp.2005.10.015.

Rapp, M., F.-J. Lübken, A. Müllemann, G. E. Thomas, and E. J. Jensen (2002), Small-scale temperature variations in the vicinity of NLC: Experimental and model results, *J. Geophys. Res.*, *107*(D19), 4392, doi:10.1029/2001JD001241.

Rong, P. P., J. M. Russell III, M. E. Hervig, and S. M. Bailey (2012), The roles of temperature and water vapor at different stages of the polar mesospheric cloud season, *J. Geophys. Res.*, *117*, D04208, doi:10.1029/2011JD016464.

Rusch, D. W., G. E. Thomas, W. McClintock, A. W. Merkel, S. M. Bailey, J. M. Russell III, C. E. Randall, C. Jeppesen, and M. Callan (2009), The cloud imaging and particle size experiment on the aeronomy of ice in the mesosphere mission: Cloud morphology for the northern 2007 season, *J. Atmos. Sol. Terr. Phys.*, *71*, 356–364, doi:10.1016/j.jastp.2008.11.005.

Russell, J. M., III, et al. (2009), Aeronomy of Ice in the Mesosphere (AIM): Overview and early science results (2009), *J. Atmos. Terr. Phys.*, *71*(3–4), 289–299, doi:10.1016/j.jastp.2008.08.011.

Russell, J. M., III, P. Rong, S. M. Bailey, M. E. Hervig, and S. V. Petelina (2010), Relationship between the summer mesopause and polar mesospheric cloud heights, *J. Geophys. Res.*, *115*, D16209, doi:10.1029/2010JD013852.

Schöch, A. (2007), Thermal structure and gravity waves in the Arctic middle atmosphere above ALOMAR (69.3°N, 16.0°E), PhD thesis, Leibniz-Inst. for Atmos. Phys., Kühlungsborn, Germany. [Available at http://www.iap-kborn.de/Thesis-Master-Diploma-PhD.64.0.html?&L=1.]

Seele, C., and P. Hartogh (1999), Water vapor of the polar middle atmosphere: Annual variation and summer mesosphere conditions as observed by ground-based microwave spectroscopy, *Geophys. Res. Lett.*, *26*, 1517–1520, doi:10.1029/1999GL900315.

Stevens, M. H., et al. (2010), Tidally induced variations of polar mesospheric cloud altitudes and ice water content using a data assimilation system, *J. Geophys. Res.*, *115*, D18209, doi:10.1029/2009JD013225.

Summers, M. E., R. R. Conway, C. R. Englert, D. E. Siskind, M. H. Stevens, J. M. Russell III, L. L. Gordley, and M. J. McHugh (2001), Discovery of a water vapor layer in the arctic summer mesosphere: Implications for polar mesospheric clouds, *Geophys. Res. Lett.*, *28*(18), 3601–3604, doi:10.1029/2001GL013217.

Thayer, J. P., M. Rapp, A. J. Gerrard, E. Gudmundsson, and T. J. Kane (2003), Gravity wave influences on Arctic mesospheric clouds as determined by a Rayleigh lidar at Sondrestrom, Greenland, *J. Geophys. Res.*, *108*(D8), 8449, doi:10.1029/2002JD002363.

Toon, O. B., R. P. Turco, J. Jordan, J. Goodman, and G. Ferry (1989), Physical processes in polar stratospheric clouds, *J. Geophys. Res.*, *94*, 11,359–11,380.

Turco, R. P., O. B. Toon, R. C. Whitten, R. G. Keesee, and D. Hollenback (1982), Noctilucent clouds: Simulation studies of their genesis, properties and global influences, *Planet. Space Sci.*, *30*, 1147–1181, doi:10.1016/0032-0633(82)90126-X.

Waters, J. W., et al. (2006), The Earth Observing System Microwave Limb Sounder (EOS MLS) on the Aura satellite, *IEEE Trans. Geosci. Remote Sens.*, *44*(5), 1075–1092, doi:10.1109/TGRS.2006.873771.

Witt, G. (1962), Height, structure, and displacements of noctilucent clouds, *Tellus*, *14*, 1–8, doi:10.1111/j.2153-3490.1962.tb00115.x.